

Physics-Aware Human-Object Rendering from Sparse Views via 3D Gaussian Splatting

Weiquan Wang¹, Jun Xiao¹, Yueting Zhuang¹, Long Chen^{2*}
¹Zhejiang University ²Hong Kong University of Science and Technology
 wqwangcs@zju.edu.cn; longchen@ust.hk

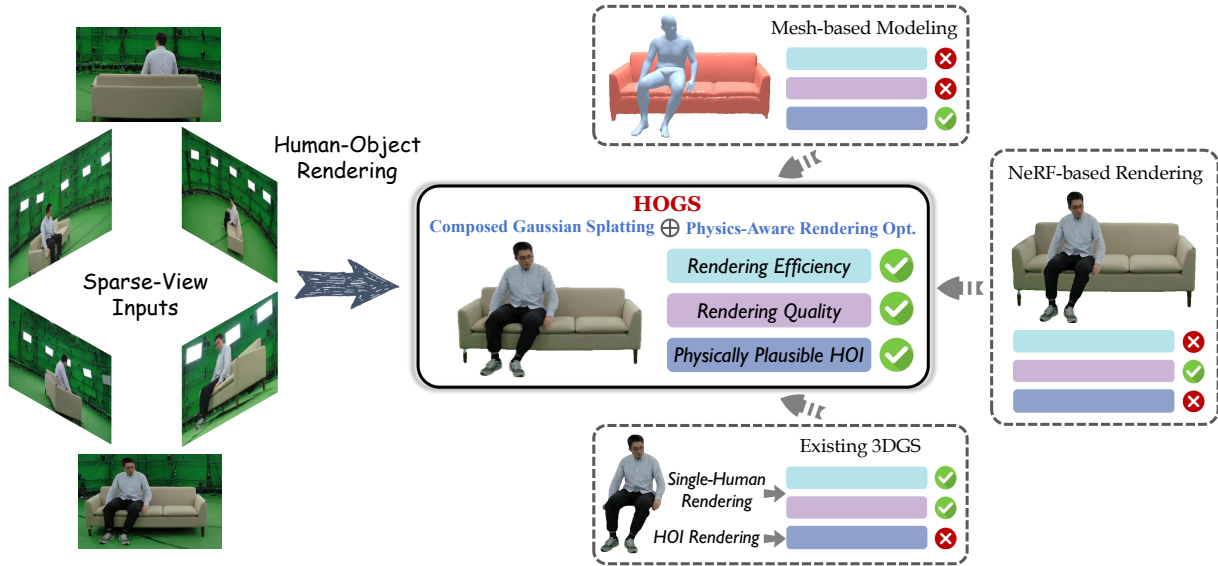


Figure 1. Comparison of state-of-the-art sparse-view HOI rendering methods. Mesh-based methods have limitations in rendering efficiency and quality; NeRF-based methods show weaknesses in rendering efficiency and physically plausible HOI; and existing 3DGS methods lack effective HOI handling despite decent single-human rendering performance. Our proposed HOGS significantly improves high-quality, efficiency, and physically plausible HOI rendering simultaneously.

Abstract

Rendering realistic human-object interactions (HOIs) from sparse-view inputs is challenging due to occlusions and incomplete observations, yet crucial for various real-world applications. Existing methods always struggle with either low rendering qualities (e.g., visual fidelity and physically plausible HOIs) or high computational costs. To address these limitations, we propose **HOGS** (Human-Object Rendering via 3D Gaussian Splatting), a novel framework for efficient and physically plausible HOI rendering from sparse views. Specifically, HOGS combines 3D Gaussian Splatting with a physics-aware optimization process. It incorporates a Human Pose Refinement module for accurate pose estimation and a Sparse-View Human-Object Contact Prediction module for efficient contact region identification. This combination enables coherent joint rendering of human and object Gaussians while enforcing physically plau-

sible interactions. Extensive experiments on the HODome dataset demonstrate that HOGS achieves superior rendering quality, efficiency, and physical plausibility compared to existing methods. We further show its extensibility to hand-object grasp rendering tasks, presenting its broader applicability to articulated object interactions.

1. Introduction

Rendering human-object interactions (HOIs) is crucial for various applications [21, 30, 33, 38]. However, accurately rendering HOIs from *sparse views* remains challenging yet pivotal for real-world deployment where dense multi-view setups are impractical [47, 79]. For instance, safety-critical autonomous driving with limited sensors and urban occlusions [14, 65], performance-analyzing sports analytics from sparse broadcast views [15], and resource-constrained mo-

ble VR/AR for immersive experiences [7, 52] all necessitate efficient and high-quality sparse-view HOI rendering.

Meanwhile, HOI rendering has witnessed significant progress within recent years [5, 25, 26, 63]. Early approaches rely on 3D mesh reconstruction combined with per-frame texture mapping [10, 12, 56], often incorporating physical optimizations to enforce plausible contact between the reconstructed human and object meshes (*i.e.*, **physically plausible**). While they provide basic visual fidelity, they are susceptible to occlusions and incomplete textures. These challenges will be even exacerbated in sparse-view settings, which limits their effectiveness in real scenarios. In light of these issues, more advanced rendering techniques are proposed to enhance HOI rendering, among which neural rendering techniques [26, 36, 62] demonstrate significant gains in **rendering quality**. A common strategy for neural HOI rendering involves utilizing a layer-wise NeRF pipeline to represent and render both human and object [25, 75], enabling free-viewpoint rendering. Despite the impressive visual fidelity achievable, this type of approach inherently demands dense multi-view inputs and incurs substantial computational overhead, limiting its practicality for real-time applications. Moreover, even with the adoption of layered representations to disentangle human and object, these pipelines generally lack dedicated mechanisms to ensure physically plausible interactions in intricate HOI scenarios.

To tackle the computational limitations of NeRF-based methods, recent research has explored 3D Gaussian Splatting (3DGS) [28] as a powerful alternative, offering remarkable **rendering efficiency** for photo-realistic rendering of both static and dynamic scenes [13, 57, 61]. This explicit Gaussian representation provides robustness to sparse views by efficiently integrating limited information and minimizing reconstruction ambiguity [9, 42, 46, 77]. Building upon these strengths, 3DGS has been successfully applied to dynamic human modeling, achieving high-quality reconstruction of animatable human avatars [20, 29, 37]. Despite these advancements, existing 3DGS-based methods predominantly focus on single-human rendering and haven't explored complex interactions between humans and objects.

In this paper, we propose **HOGS (Human-Object Rendering via 3D Gaussian Splatting)**, a novel framework for efficient and physically plausible rendering of HOIs, particularly from sparse-view inputs. As illustrated in Fig. 1, HOGS addresses the limitations of existing methods by combining efficient joint rendering of human and object Gaussians with a physics-aware optimization process. Notably, HOGS achieves high **rendering efficiency**, **rendering quality**, and **physically plausible** HOIs simultaneously, a harmony that previous approaches have not attained.

Structurally, HOGS encompasses two primary components: **Composed Gaussian Splatting** and **Physics-Aware Rendering Optimization**. The Composed Gaussian Splat-

ting component is proposed to achieve efficient and high-quality HOI rendering, tackling the computational burden of NeRF-based approaches by capitalizing on the efficiency of 3D Gaussian Splatting. A key aspect of Composed Gaussian Splatting is the *Human-Object Deformation* process, which unifies the representation of both dynamic humans and static objects within a single 3DGS framework. Furthermore, to overcome the challenges of sparse-view inputs, HOGS incorporates a *Sparse-View Human Pose Refinement* module. This module enhances the accuracy of human pose estimation and LBS transformations using multi-view consistency, ensuring robust human modeling even under sparse-view conditions.

Complementing Composed Gaussian Splatting, HOGS further ensures physically plausible HOIs with its Physics-Aware Rendering Optimization. Recognizing the absence of dedicated physical interaction mechanisms in existing 3DGS methods, this component addresses the issues of interpenetration and unrealistic contact. The core mechanism lies in incorporating *Attraction and Repulsion Losses* into the optimization process, directly enforcing physical plausibility. To improve optimization efficiency, HOGS employs a *Sparse-View Human-Object Contact Prediction* module. This module predicts contact regions leveraging multi-view information, allowing HOGS to focus the computation of physical losses only on these relevant contact regions.

Our main contributions are summarized as follows:

- We systematically analyze the advantages and weaknesses of state-of-the-art HOI rendering methods.
- We present HOGS, a novel framework for efficient and high-quality rendering of complex HOIs from sparse-view inputs, unifying dynamic human and static object representations within a 3DGS framework.
- We introduce a physics-aware rendering optimization that operates directly on Gaussian representations to enforce physically plausible interactions, preventing interpenetration and promoting realistic contact within HOIs.
- To enhance HOI rendering, we develop two key modules: Pose Refinement for accurate LBS transformations based on multi-view consistency; and Sparse-View Contact Prediction for accurate contact prediction of HOI.
- We demonstrate the effectiveness of HOGS on HOI rendering [75] and further extend it to hand-object grasp rendering [50], showcasing its applicability to articulated interactions rendering.

2. Related Work

Free Viewpoint Rendering (FVR). FVR, synthesizing novel views of a scene, is a long-standing challenge in computer vision [24, 58, 69, 72, 74]. Traditional methods generate novel views by blending or warping input views based on geometric constraints [2, 59, 60], but they are limited to viewpoints near the input cameras. Recent

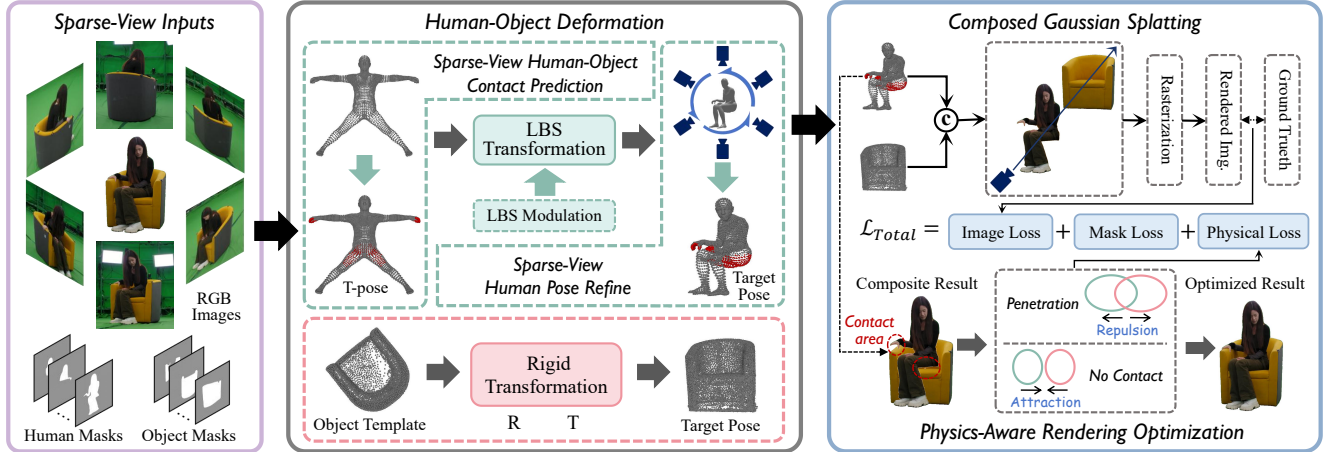


Figure 2. HOGS pipeline. Given some sparse views of a dynamic HOI scene, HOGS first deforms human and object representations using a *Human-Object Deformation* process, which includes LBS for humans and rigid transformations for objects, along with a Human Pose Refinement module to enhance target pose accuracy. Deformed human and object Gaussians are then composed into a unified 3D space to form the *Composed Gaussian Splatting*. Finally, this composed result is optimized with a *Physics-Aware Rendering Optimization* process, which incorporates a Human-Object Contact Prediction module and a physical loss to enforce physically plausible interactions.

studies have shifted towards using neural representations, which enable higher-quality FVR both for static and dynamic scenarios [8, 11, 71, 80]. However, these methods typically require dense views for higher-quality rendering. In real-world applications, dense-view setups are impractical or impossible, due to occlusions or limited camera setups [31, 73, 77]. To this end, we focus on high-quality HOI rendering from sparse views.

Differentiable Rendering of Radiance Fields. Differentiable rendering has significantly advanced FVR [1, 49, 70]. NeRF [43] pioneered this field by representing scenes as implicit functions [32, 45, 81]. While NeRF provides impressive rendering results, its reliance on ray marching remains a computational bottleneck. In contrast, 3DGS [28] employs explicit 3D Gaussians for efficient rendering, rapidly emerging as a powerful technique for real-time rendering [40, 51, 82]. Leveraging its inherent efficiency, 3DGS has been successfully extended to dynamic human modeling, enabling the impressive reconstruction of human avatars [20, 29, 44]. However, these methods mainly focus on single humans and do not explicitly address the complex interactions inherent in multi-object scenes. In this work, we extend 3DGS to jointly model and render HOIs, enabling efficient and high-quality complex scenes rendering.

Physics-aware HOI Rendering. Enforcing physically plausible interactions is crucial for realistic HOI rendering. Traditional methods often incorporate physical optimizations into mesh-based reconstructions to ensure human-object plausible contact, which typically employ penalty terms [17, 18, 76], specific constraints [3, 19], or physical criteria [16, 23]. However, these techniques, designed for static mesh vertices, are not directly applicable to ex-

plicit Gaussian representations, which relies on dynamically changing Gaussian primitives in both numbers and positions during optimization. To bridge this gap, our work introduces a physics-aware rendering optimization specifically designed for 3DGS, leveraging attraction and repulsion losses to enforce physically plausible HOIs and enhance rendering quality. Furthermore, we incorporate a sparse-view contact prediction module to improve the efficiency of physics-based optimization by focusing computation on relevant contact regions.

3. Methodology

Given a scene of HOIs captured by sparse RGB cameras, our HOGS consists of three main stages: 1) We first deform human and object representations using a *Human-Object Deformation* process (Sec. 3.1). 2) We then compose the deformed human and object Gaussians into a unified 3D space to form a *Composed Gaussian* representation of the HOI (Sec. 3.2). 3) Finally, we optimize this composed representation with a *Physics-Aware Rendering Optimization* process (Sec. 3.3). The pipeline of HOGS is shown in Fig 2.

3.1. Human-Object Deformation

To accurately represent HOIs, we first deform both the human and the object from initial states to their respective target states. Human deformation includes applying standard LBS transformations, adding an LBS modulation to capture finer details, and further refining the target pose through a refinement module. The object deformation is simplified by treating the object as rigid and estimating its rigid transformation with respect to a pre-scanned template.

LBS Transformation. LBS is commonly employed in hu-

man rendering to deform human representations [20, 29, 37, 44]. Following this approach, we utilize LBS to transform human Gaussians. We adopt the SMPL-H [54] model, a parametric 3D human body model that extends SMPL to incorporate high-fidelity hand details. 3D Gaussians are initialized by placing their means \mathbf{p}^c at the SMPL-H mesh vertices and assigning each an initial covariance Σ^c . These initial Gaussians, defined in the canonical T-pose space, are then transformed to the posed space via LBS. Specifically, the transformed mean \mathbf{p}^t and covariance Σ^t are given by:

$$\mathbf{p}^t = \sum_{k=1}^K w_k (\mathbf{R}_k \mathbf{p}^c + \mathbf{t}_k) + \mathbf{b}, \quad (1)$$

$$\Sigma^t = \left(\sum_{k=1}^K w_k \mathbf{R}_k \right) \Sigma^c \left(\sum_{k=1}^K w_k \mathbf{R}_k \right)^T, \quad (2)$$

where K is the number of joints, w_k is the LBS weight associated with joint k , \mathbf{b} is a global translation vector, and \mathbf{R}_k and \mathbf{t}_k represent the rotation matrix and translation vector. **LBS Modulation.** While LBS provides an efficient way to deform the human representation, it still struggles to capture fine-grained details and subtle deformations. Inspired by previous works that learn LBS weight fields for detailed human modeling [20, 22, 35, 36, 48], we introduce an LBS modulation to refine the initial LBS weights derived from the SMPL-H model. Specifically, we leverage the pre-computed SMPL-H weights as a strong prior and employ an MLP Φ_{lbs} to modulate each LBS weight. Given a 3D Gaussian centered at \mathbf{p}^c in the canonical space, we first apply a positional encoding $\gamma(\mathbf{p}^c)$ to its position. The MLP then outputs a modulation vector $\mathbf{m} = \Phi_{lbs}(\gamma(\mathbf{p}^c))$, where each element m_k corresponds to the modulation factor for the k -th LBS weight. The final LBS weight w_k is computed through a softmax function:

$$w_k = \text{softmax}(w_k^{\text{SMPL-H}} + m_k) \quad (3)$$

where $w_k^{\text{SMPL-H}}$ is the LBS weight derived from the nearest SMPL-H vertex for joint k . This approach modulates LBS weights efficiently, capturing finer details of deformations. **Sparse-View Human Pose Refinement.** As mentioned, LBS transformation relies on a target human pose. However, in sparse-view scenarios, human-object occlusions degrade the accuracy of this pose estimation. To this end, we introduce a human pose refinement module, which extends HMR [27] to the sparse-view setting and incorporates a dynamic view weighting mechanism to handle occlusions. As shown in Fig. 3, we first regress initial pose and shape estimations from multi-view images using a regressor, and then refine estimations through sparse-view optimization. Finally, the parameters of both the regressor and the sparse-view optimization process are jointly optimized.

(a) HMR Regressor. We first use an off-the-shelf regressor [27] to obtain initial pose and shape parameters $\mathbf{H}_{\text{reg}}^i = \{\theta_{\text{reg}}^i, \beta_{\text{reg}}^i\}$ from N views, where θ_{reg}^i and β_{reg}^i represent SMPL-H parameters of i -th view. Unlike single-view

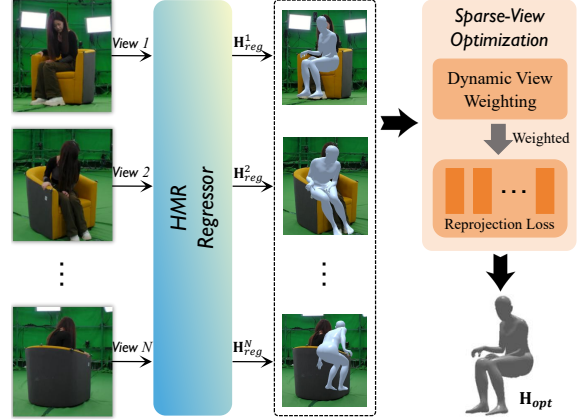


Figure 3. Illustration of sparse-view human pose refinement module. Sparse-view RGB images are processed by an HMR regressor to obtain initial pose and shape estimations. These estimations are then refined through a sparse-view optimization with a dynamic view weighting approach.

HMR, we process multiple views simultaneously, extracting consistent pose and shape information across N views. We pre-train the regressor using a 2D joint reprojection loss $\mathcal{L}_{2D} = \sum_{i=1}^N \|J_{\text{reg}}^i - J_{\text{gt}}^i\|$, where J_{reg}^i and J_{gt}^i are the regressed and ground truth 2D joints of i -th view, respectively.

(b) Sparse-View Optimization. Building upon the pre-trained regressor, we perform sparse-view optimization to refine \mathbf{H}_{reg} . This process is inspired by SMPLify [6] and is adapted for sparse-view scenarios by incorporating multi-view consistency and dynamic view weighting.

For i -th view, we define a *per-view cost function* that encourages the 2D projection of the estimated 3D joints $P(\mathbf{H})$ to align with the initially regressed 2D joints \mathbf{H}_{reg} :

$$\mathcal{E}_i = \|P(\mathbf{H}) - J_{\text{reg}}^i\|^2 + \lambda_\theta E_\theta(\theta) + \lambda_\beta E_\beta(\beta), \quad (4)$$

where $E_\theta(\theta)$ and $E_\beta(\beta)$ represent regularization terms which constrain the pose and shape parameters [34].

To handle the varying reliability of different views due to occlusions in sparse-view scenarios, we introduce *dynamic view weights* d_i for i -th view. We first estimate the occlusion rate $E_i = 1 - V_i/K$, where K is the total number of joints. V_i represents the number of visible joints from i -th view, which is determined by checking if the 2D projected joints $P(\mathbf{H})$ falling within the human mask of i -th view. E_i is used to compute the dynamic weights d_i by a softmax function $d_i = \text{softmax}(-\alpha E_i)$, where α is a sensitivity factor, which is set to 5.

The total cost function for sparse-view optimization is then defined as the weighted sum of \mathcal{E}_i :

$$\mathcal{E}_{\text{total}} = \sum_{i=1}^N d_i \cdot \mathcal{E}_i. \quad (5)$$

Minimizing $\mathcal{E}_{\text{total}}$ yields the optimized pose and shape parameters $\mathbf{H}_{\text{opt}} = \{\theta_{\text{opt}}, \beta_{\text{opt}}\}$, and corresponding 3D joints $\mathbf{p}_{\text{opt}}^i$ for each view.

(c) Joint Training. We employ a combined loss function for joint training:

$$\mathcal{L}_{\text{HPR}} = \lambda_1 \mathcal{L}_{2D} + \lambda_2 \mathcal{L}_{3D} + \lambda_3 \mathcal{L}_{\text{H}}, \quad (6)$$

where $\mathcal{L}_{3D} = \sum_{i=1}^N \|\mathbf{p}_{\text{gt}}^i - \mathbf{p}_{\text{opt}}^i\|$, $\mathcal{L}_{\text{H}} = \sum_{i=1}^N \|\mathbf{H}_{\text{reg}}^i - \mathbf{H}_{\text{opt}}\|$. λ_1 , λ_2 , and λ_3 are set to 5, 5, 0.001, respectively. Crucially, this joint training process enables the parameters of both the HMR regressor and the sparse-view optimization to be optimized simultaneously.

Object Deformation. Objects involved in HOIs are typically rigid. To model object deformation, we follow prior work [64, 75], only estimating its rotation $R_t \in SO(3)$ and rigid translation $T_t \in \mathbb{R}^3$ with respect to its template mesh $\mathcal{M}_{\text{temp}}$. As shown in Fig. 2, given a pre-scanned object template, we employ the rigid iterative closest point technique [4] to compute the rigid transformation between the per-frame markers and the template. This rigid transformation, composed of rotation R_t and translation T_t , directly yields the target pose of object mesh \mathcal{M}_{tar} . This per-frame estimation allows us to track the rigid motion of objects throughout the RGB input sequence.

3.2. Composed Gaussian Splatting

Building upon 3DGS, we extend it to jointly render humans and objects within a single scene. Instead of treating the entire scene as one homogeneous Gaussian set, we separate it into two subsets: 1) **Human Gaussians**: For the human, each vertex of the SMPL-H model is converted into a 3D Gaussian, forming the human Gaussian set $\{\mathcal{G}_i^h = \mathcal{N}(\mathbf{x}_i; \mu_i^h, \Sigma_i^h)\}$, where \mathbf{x} follows a normal distribution with mean μ and covariance Σ . The human Gaussian parameters μ_i^h and Σ_i^h are updated frame-by-frame based on the refined pose and shape parameters from Sec. 3.1, ensuring accurate motion tracking of the articulated human body. 2) **Object Gaussians**: For the object, the vertices of the target pose of object mesh \mathcal{M}_{tar} are used to initialize the means of the object Gaussians. Specifically, each vertex of \mathcal{M}_{tar} becomes the mean μ_j^o of an object Gaussian \mathcal{G}_j^o , with an assigned initial covariance Σ_j^o . Then, the human and object Gaussian sets are merged into a unified set: $\mathcal{G} = \{\mathcal{G}_i^h\} \cup \{\mathcal{G}_j^o\}$.

Then, the combined Gaussian set \mathcal{G} is projected into the 2D plane. The covariance matrix Σ of each 3D Gaussian is transformed to its projected 2D covariance Σ' as follows:

$$\Sigma' = \mathbf{J} \mathbf{W} \Sigma \mathbf{W}^T \mathbf{J}^T, \quad (7)$$

where \mathbf{W} is the world-to-camera transformation matrix, \mathbf{J} is the Jacobian of the affine approximation of the projective transformation. The projected Gaussians are blended using α -compositing to generate the rendered image, which

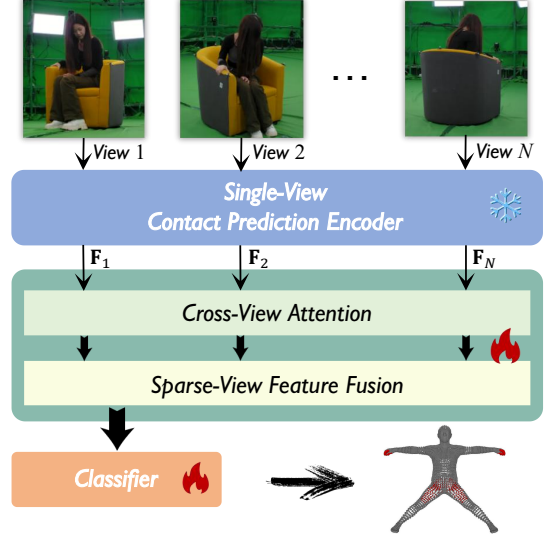


Figure 4. The workflow of sparse-view contact prediction method. Given sparse-view images, a single-view contact prediction encoder outputs per-view features, which are then processed by cross-view attention and feature fusion to produce a sparse-view fused feature. Finally, a classifier predicts the contact regions corresponding to the SMPL-H vertices.

is compared with the ground-truth image using $\mathcal{L}_{\text{image}}$ loss. This composed Gaussian splatting process leverages the flexibility of Gaussian representations to capture dynamic human motion and static objects within the same scene.

3.3. Physics-Aware Rendering Optimization

To ensure physically plausible HOI rendering, we introduce a two-step rendering optimization process. Firstly, we predict potential human-object contact regions using a novel sparse-view human-object contact prediction module. This prediction yields a set of human Gaussians corresponding to the contact regions. Secondly, leveraging these predicted regions, we perform a physical optimization on the composed Gaussian splatting result to enforce physical constraints.

3.3.1. Sparse-View Human-Object Contact Prediction

Directly compositing Gaussians (as in Sec. 3.2) may lead to physically implausible interactions at human-object contact regions. Optimizing this issue for rendering HOIs requires first identifying the location of human-object contact regions. To this end, we propose a sparse-view contact prediction module, which is illustrated in Fig. 4.

Given images captured from N views, we first extract per-view HOI features using a single-view contact prediction encoder. Specifically, we utilize the architecture from DECO [66], excluding the final MLP layer, to obtain per-view features $\mathbf{F} = \{\mathbf{F}_i\}_{i=1}^N \in \mathbb{R}^{N \times D}$, where D is the feature dimension. \mathbf{F} is then processed by a cross-view atten-

tion module, which outputs $F_{\text{att}} \in \mathbb{R}^{N \times D}$ is computed as:

$$F_{\text{att}} = \text{softmax} \left(\frac{QK^T}{\sqrt{D}} \right) V, \quad (8)$$

where $Q = FW_Q$, $K = FW_K$, and $V = FW_V$ represent the query, key, and value matrices derived from the multi-view features F . $W_Q, W_K, W_V \in \mathbb{R}^{D \times D}$ are learnable transformation matrices. F_{att} is then fed to a sparse-view feature fusion module to produce the fused feature $F_{\text{fuse}} \in \mathbb{R}^D$. Finally, F_{fuse} is passed through a classifier to obtain the probability $\mathcal{P} \in \mathbb{R}^{6890}$ of each SMPL-H vertex being in contact. The set of indices of contact vertices is defined as $\mathcal{C} = \{i \mid \mathcal{P}_i > \tau\}$, where $\tau = 0.5$ is a threshold. We compare \mathcal{C} with the ground truth using a cross-entropy loss. Corresponding to the HOI contact region, \mathcal{C} will be used in subsequent physical optimization.

During the training process, the parameters of the single-view contact prediction encoder are frozen to leverage the knowledge of the DECO. Only the parameters of the cross-view attention module and the classifier are updated.

3.3.2. Physics-Aware Optimization

Having identified the human-object contact regions through contact prediction, which yields the set of indices \mathcal{C} corresponding to the human Gaussians, we now perform a physics-aware optimization on these regions within the composed Gaussian splatting framework (Fig. 2). This optimization enforces physical plausibility by minimizing two distinct loss terms: an Attraction Loss and a Repulsion Loss, which guide the human and object Gaussians towards physically plausible configurations.

Attraction Loss. To encourage closer proximity between the human and object Gaussians at the contact regions, we define an attraction loss. Specifically, this loss is computed by considering the distances between the human Gaussians corresponding to the contact vertices \mathcal{C} and all object Gaussians. Let $\{\mathcal{G}_i^h = G(\mathbf{x}_i; \mu_i^h, \Sigma_i^h)\}_{i \in \mathcal{C}}$ represent the set of human Gaussians corresponding to the contact vertices \mathcal{C} , and $\{\mathcal{G}_j^o = G(\mathbf{x}_j; \mu_j^o, \Sigma_j^o)\}_{j=1}^{N_o}$ represent the set of all N_o object Gaussians. The attraction loss is then defined as:

$$\mathcal{L}_{\text{attr}} = \frac{1}{|\mathcal{C}|} \sum_{i \in \mathcal{C}} \min_{1 \leq j \leq N_o} \|\mu_i^h - \mu_j^o\|_2 + \frac{1}{N_o} \sum_{j=1}^{N_o} \min_{i \in \mathcal{C}} \|\mu_j^o - \mu_i^h\|_2. \quad (9)$$

This loss term effectively pulls the interacting regions of the human and object Gaussians closer, promoting a more physically plausible interaction by reducing unnatural gaps.

Repulsion Loss. In addition to addressing unnatural gaps between the human and object, intuitive physics dictates that two objects cannot occupy the same 3D space, a phenomenon known as *penetration*. Therefore, we introduce a repulsion loss to penalize the interpenetration of human and object Gaussians. Our approach leverages Signed Distance

Fields (SDFs) for penetration detection. While a direct approach would be to compute SDFs from the human/object Gaussians, this incurs a significant computational burden. As the Gaussians dynamically change in both numbers and positions during optimization, frequent recomputation of the SDF would be required. To mitigate this computational cost, we exploit the fact that the object is static and can be represented by a fixed target mesh \mathcal{M}_{tar} (Sec. 3.1). Consequently, we pre-compute the SDF of \mathcal{M}_{tar} only once before 3DGS optimization, significantly improving efficiency.

Specifically, we construct a uniform voxel grid with a size of $256 \times 256 \times 256$ that spans a padded bounding box of \mathcal{M}_{tar} . Each voxel cell’s center $c_i \in \mathbb{R}^3$ stores the signed distance δ_i to the nearest surface point on \mathcal{M}_{tar} . The sign of δ_i indicates whether the cell center is inside (negative) or outside (positive) the object. To determine the penetration of a human Gaussian \mathcal{G}_i^h (corresponding to a contact vertex index $i \in \mathcal{C}$) into the object, we evaluate the SDF at its mean μ_i^h . We use trilinear interpolation within the voxel grid to obtain a continuous signed distance value $\delta(\mu_i^h)$ and the corresponding interpolated normal vector $\mathbf{n}(\mu_i^h)$ at μ_i^h . Then, the repulsion loss is defined as:

$$\mathcal{L}_{\text{rep}} = \frac{1}{|\mathcal{C}|} \sum_{i \in \mathcal{C}} \max(0, -\delta(\mu_i^h)) \|\mathbf{n}(\mu_i^h)\|_2^2, \quad (10)$$

where we only penalize negative signed items.

Total Loss. As shown in Fig. 2, our overall training objective of composed Gaussian splatting is to minimize:

$$\mathcal{L}_{\text{total}} = \mathcal{L}_{\text{image}} + \lambda_{\text{ssim}} \mathcal{L}_{\text{ssim}} + \lambda_{\text{lpips}} \mathcal{L}_{\text{lpips}} + \lambda_{\text{mask}} \mathcal{L}_{\text{mask}} + \lambda_{\text{attr}} \mathcal{L}_{\text{attr}} + \lambda_{\text{rep}} \mathcal{L}_{\text{rep}}, \quad (11)$$

where the mask loss $\mathcal{L}_{\text{mask}}$ is computed based on the human-object mask [75], and the rendered image is compared with the ground-truth image using $\mathcal{L}_{\text{image}}$ (Sec. 3.2), SSIM loss [68], and the LPIPS loss [78].

4. Experiments

4.1. Experimental Setup

We evaluated HOGS on the HOI rendering dataset HODome [75] and extended our method to hand-object grasp rendering task with the MANUS-Grasps dataset [50]. HODome provides 76 RGB videos of HOIs, covering 23 diverse 3D objects and 10 subjects. It provides human and object masks, object templates, camera parameters, and SMPL-H parameters. Following HODome, we used 6 views for training and evaluated on the remaining views. Due to the scarcity of suitable datasets for HOI rendering, we extended our evaluation to the hand-object grasp dataset MANUS-Grasps to further demonstrate the applicability of HOGS to articulated interactions. MANUS-Grasps is captured by 53 RGB cameras, providing nearly full 360° cov-

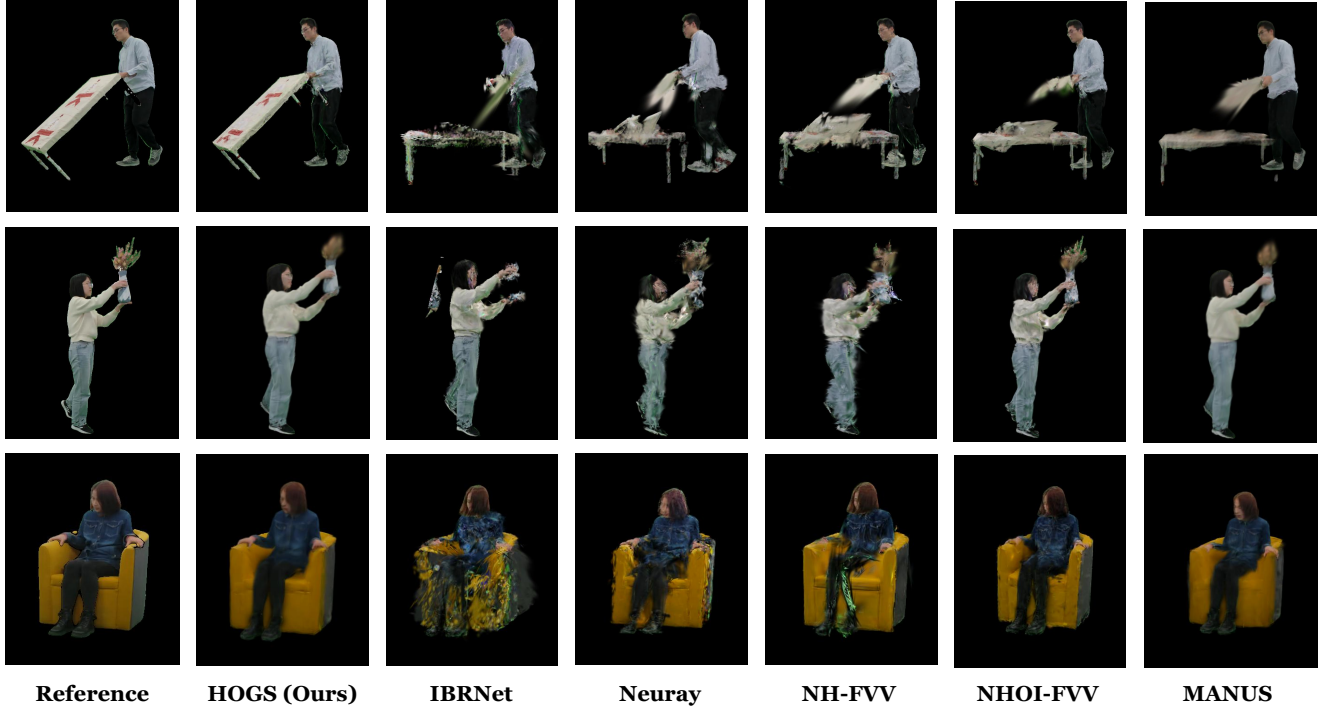


Figure 5. Qualitative evaluation of novel view synthesis for HOI rendering on the HODome dataset. HOGS demonstrates superior visual fidelity and more accurate representation of human-object interactions compared to existing methods.

erage of grasp sequences. Similar to HODome, MANUS-Grasps provides hand and object segmentation masks and camera parameters. As MANUS-Grasps does not provide pre-scanned object templates, we replace our object deformation module with the well-trained object Gaussians from MANUS as our initial object Gaussians. To verify sparse-view rendering quality, we selected 6 evenly distributed camera views from available views for hand-object rendering. The implementation details are shown in the **appendix**.

4.2. Results

Comparison Methods. We compared our HOGS with three categories of state-of-the-art rendering approaches: mesh-based blending (NeuralHumanFVV [63]), NeRF-based rendering (IBRNet [67], NeuRay [39], and NeuralHOIFVV [75]), and 3DGS-based rendering (MANUS [50]). Following NeuralDome [75], we reported the average metric values of all HOI sequences. More details about comparison methods are shown in the appendix.

Quantitative Results. As shown in Table 1, we quantitatively evaluated HOGS on the HODome dataset. HOGS demonstrates significant advantages in both rendering quality and efficiency compared to existing methods. In terms of rendering efficiency, HOGS achieves a significantly higher frame rate (179 FPS) than other methods, highlighting the benefit of explicit composed Gaussian representation for real-time rendering. Regarding rendering quality, HOGS

Table 1. Quantitative results of novel view synthesis on HODome dataset. NH-FVV indicates the NeuralHumanFVV method and NHOI-FVV indicates the NeuralHOIFVV method. We use **red** and **yellow** text to denote the best and second-best results of each metric respectively.

Category	Method	PSNR \uparrow	SSIM \uparrow	LPIPS \downarrow	FPS \uparrow
Mesh-based	NH-FVV	21.69	0.914	-	12
	IBRNet	21.43	0.892	-	-
NeRF-based	NeuRay	23.34	0.909	-	2
	NHOI-FVV	23.10	0.912	-	1
3DGS-based	MANUS	27.28	0.936	0.062	165
	HOGS (Ours)	30.68	0.953	0.028	176

achieves state-of-the-art rendering quality with the PSNR of 30.68 dB, the SSIM of 0.953, and the LPIPS of 0.028. These results demonstrate the effectiveness of our proposed HOGS for high-quality HOI rendering. For MANUS-Grasps dataset, the results are detailed in the Appendix.

Qualitative Results. As shown in Fig. 5, we present qualitative comparisons of HOGS with existing methods. HOGS achieves superior rendering quality, generating novel views that closely resemble the reference images. In contrast, the mesh-based method (NH-FVV) struggles with occlusions, resulting in noticeable artifacts and incomplete geom-

Table 2. Ablation results on the HODome dataset. We incrementally add the proposed modules to show the effect of each component in HOGS. SV denotes sparse-view. We use red and yellow text to denote the best and second-best results of each metric respectively.

Method	PSNR \uparrow	SSIM \uparrow	FPS \uparrow
Baseline	26.96	0.928	179
+ LBS Modulation	26.98	0.928	175
+ SV Human Pose Refinement	27.40	0.931	174
+ Composed Gaussian Splatting	29.12	0.944	171
+ Attraction Loss	29.95	0.951	165
+ Repulsion Loss	30.85	0.956	157
+ SV Contact Prediction	30.47	0.949	162

etry. NeRF-based methods (IBRNet, Neuray, and NHOI-FVV) also exhibit various artifacts, including blurry textures and geometric distortions. While the 3DGS-based method, MANUS, captures the overall human-object structure and provides reasonable rendering results, it lacks fine-grained details, especially in the HOI regions.

Extensibility of HOGS. To further demonstrate the extensibility of HOGS, we conducted experiments on the hand-object grasping dataset MANUS-Grasps. As shown in Fig. 6, HOGS successfully renders various hand-object grasping scenes, demonstrating its ability to handle interactions involving articulated human hands and diverse object shapes. These results highlight the broader applicability of our pipeline to articulated interactions.

4.3. Ablation Studies

To validate the effectiveness of each component in HOGS, we conducted ablation studies on a representative subject (subject01) from the HODome dataset, as shown in Table 2.

Baseline Setup. We establish a baseline that renders the human and object using separate 3D Gaussian Splatting and then combines the resulting point clouds for final rendering. In this baseline, human deformation relies solely on the LBS transformation (Sec. 3.1) with a randomly selected pose from the 6 input views as the target pose, while object deformation is performed consistently with the method detailed in Section 3.1.

Incremental Module Analysis. We incrementally added our proposed modules to the baseline and evaluated the novel view synthesis results. As shown in Table 2, the rendering quality consistently improves with the inclusion of each module, achieving the best results when the repulsion loss is included. This progressive improvement clearly demonstrates the effectiveness of our designed modules.

Impact of Sparse-View Contact Prediction Module. It is noteworthy that incorporating the sparse-view contact pre-



Figure 6. Extensibility of HOGS. Rendering results of diverse hand-object grasping scenarios from the MANUS-Grasps dataset.

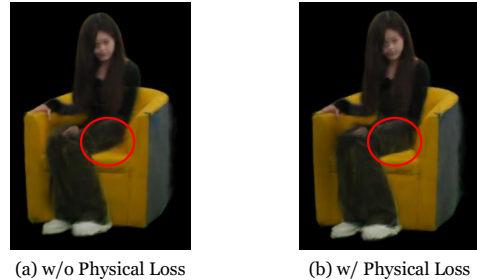


Figure 7. Effect of physical loss. (a) Without physical loss, the rendered human floats above the chair, exhibiting a lack of physical contact. (b) Incorporating physical loss results in plausible contact and a more physically consistent rendering.

diction module leads to a slight decrease in rendering quality but a significant increase in rendering efficiency (Table 2). This phenomenon arises from the focused scope of the physical loss computation. Without contact prediction, the physical loss terms (Eq. (9) and Eq. (10)) are applied between all human and object Gaussians, resulting in a comprehensive but computationally expensive process. However, human-object contact naturally occurs only within limited regions, involving only small subsets of human Gaussians. Therefore, the sparse-view human-object contact prediction module is crucial for efficient HOI rendering, as it allows HOGS to concentrate optimization on relevant contact regions, enhancing computational efficiency.

Effect of Physical Loss. Fig. 7 provides a qualitative comparison of rendering results with and without the proposed physical loss. As shown in Fig. 7(a), rendering without physical losses causes the human to float above the sofa, lacking plausible physical contact. Conversely, Fig. 7(b) demonstrates a significant visual improvement when physical losses are incorporated. The rendered human now exhibits plausible contact with the chair, showcasing a more realistic and physically consistent interaction. This visual evidence further validates the effectiveness of our proposed physical losses in enforcing plausible HOIs.

5. Conclusion

In this paper, we present HOGS, a novel approach for rendering realistic and physically plausible HOIs from sparse views. The key innovation lies in the integration of com-

posed Gaussian Splatting with physics-aware rendering optimization, complemented by sparse-view human pose refinement and contact prediction. This combination enables HOGS to effectively capture the intricate interplay between humans and objects, generating high-quality novel views that adhere to physical constraints. Extensive experiments demonstrate that HOGS achieves superior performance in terms of rendering quality, efficiency, and physical plausibility compared to existing methods, while also showing broader applicability to articulated object interactions.

References

- [1] Sai Praveen Bangaru, Michael Gharbi, Fujun Luan, Tzu-Mao Li, Kalyan Sunkavalli, Milos Hasan, Sai Bi, Zexiang Xu, Gilbert Bernstein, and Fredo Durand. Differentiable rendering of neural sdfs through reparameterization. In *SIGGRAPH Asia 2022 Conference Papers*, pages 1–9, 2022. 3
- [2] Aayush Bansal, Minh Vo, Yaser Sheikh, Deva Ramanan, and Srinivasa Narasimhan. 4d visualization of dynamic events from unconstrained multi-view videos. In *Proceedings of the IEEE/CVF Conference on Computer Vision and Pattern Recognition*, pages 5366–5375, 2020. 2
- [3] Peter Battaglia, Razvan Pascanu, Matthew Lai, Danilo Jimenez Rezende, et al. Interaction networks for learning about objects, relations and physics. *Advances in neural information processing systems*, 29, 2016. 3
- [4] Paul J Besl and Neil D McKay. Method for registration of 3-d shapes. In *Sensor fusion IV: control paradigms and data structures*, pages 586–606. Spie, 1992. 5
- [5] Bharat Lal Bhatnagar, Xianghui Xie, Ilya A Petrov, Cristian Sminchisescu, Christian Theobalt, and Gerard Pons-Moll. Behave: Dataset and method for tracking human object interactions. In *Proceedings of the IEEE/CVF Conference on Computer Vision and Pattern Recognition*, pages 15935–15946, 2022. 2
- [6] Federica Bogo, Angjoo Kanazawa, Christoph Lassner, Peter Gehler, Javier Romero, and Michael J Black. Keep it smpl: Automatic estimation of 3d human pose and shape from a single image. In *Computer Vision—ECCV 2016: 14th European Conference, Amsterdam, The Netherlands, October 11–14, 2016, Proceedings, Part V 14*, pages 561–578. Springer, 2016. 4
- [7] Kevin Boos, David Chu, and Eduardo Cuervo. Flashback: Immersive virtual reality on mobile devices via rendering memoization. In *Proceedings of the 14th Annual International Conference on Mobile Systems, Applications, and Services*, pages 291–304, 2016. 2
- [8] Ang Cao and Justin Johnson. Hexplane: A fast representation for dynamic scenes. In *Proceedings of the IEEE/CVF Conference on Computer Vision and Pattern Recognition*, pages 130–141, 2023. 3
- [9] Yuedong Chen, Haofei Xu, Chuanxia Zheng, Bohan Zhuang, Marc Pollefeys, Andreas Geiger, Tat-Jen Cham, and Jianfei Cai. Mvsplat: Efficient 3d gaussian splatting from sparse multi-view images. In *European Conference on Computer Vision*, pages 370–386. Springer, 2025. 2
- [10] Alvaro Collet, Ming Chuang, Pat Sweeney, Don Gillett, Dennis Evseev, David Calabrese, Hugues Hoppe, Adam Kirk, and Steve Sullivan. High-quality streamable free-viewpoint video. *ACM Transactions on Graphics (ToG)*, 34(4):1–13, 2015. 2
- [11] Yuhan Ding, Fukun Yin, Jiayuan Fan, Hui Li, Xin Chen, Wen Liu, Chongshan Lu, Gang Yu, and Tao Chen. point diffusion implicit function for large-scale scene neural representation. *Advances in Neural Information Processing Systems*, 36, 2024. 3
- [12] Mingsong Dou, Philip Davidson, Sean Ryan Fanello, Sameh Khamis, Adarsh Kowdle, Christoph Rhemann, Vladimir Tankovich, and Shahram Izadi. Motion2fusion: Real-time volumetric performance capture. *ACM Transactions on Graphics (ToG)*, 36(6):1–16, 2017. 2
- [13] Ben Fei, Jingyi Xu, Rui Zhang, Qingyuan Zhou, Weidong Yang, and Ying He. 3d gaussian splatting as new era: A survey. *IEEE Transactions on Visualization and Computer Graphics*, 2024. 2
- [14] Felipe Fernandez, Angel Sanchez, Jose F Velez, and Belen Moreno. Associated reality: A cognitive human-machine layer for autonomous driving. *Robotics and Autonomous Systems*, 133:103624, 2020. 1
- [15] Guillaume Gourmelen, Shutaro Toriya, Eiko Miya, Naohisa Shioura, and Hiroyasu Iwata. Miruoto: Sports event atmosphere visual rendering through real-time image and sound processing system. In *ACM SIGGRAPH 2024 Emerging Technologies*, pages 1–2, 2024. 1
- [16] Abhinav Gupta, Aniruddha Kembhavi, and Larry S Davis. Observing human-object interactions: Using spatial and functional compatibility for recognition. *IEEE transactions on pattern analysis and machine intelligence*, 31(10):1775–1789, 2009. 3
- [17] Mohamed Hassan, Vasileios Choutas, Dimitrios Tzionas, and Michael J Black. Resolving 3d human pose ambiguities with 3d scene constraints. In *Proceedings of the IEEE/CVF international conference on computer vision*, pages 2282–2292, 2019. 3
- [18] Mohamed Hassan, Partha Ghosh, Joachim Tesch, Dimitrios Tzionas, and Michael J Black. Populating 3d scenes by learning human-scene interaction. In *Proceedings of the IEEE/CVF Conference on Computer Vision and Pattern Recognition*, pages 14708–14718, 2021. 3
- [19] Haoyu Hu, Xinyu Yi, Zhe Cao, Jun-Hai Yong, and Feng Xu. Hand-object interaction controller (hoic): Deep reinforcement learning for reconstructing interactions with physics. In *ACM SIGGRAPH 2024 Conference Papers*, pages 1–10, 2024. 3
- [20] Shoukang Hu, Tao Hu, and Ziwei Liu. Gauhuman: Articulated gaussian splatting from monocular human videos. In *Proceedings of the IEEE/CVF Conference on Computer Vision and Pattern Recognition*, pages 20418–20431, 2024. 2, 3, 4
- [21] Chun-Hao P Huang, Hongwei Yi, Markus Höschle, Matvey Safroshkin, Tsvetelina Alexiadis, Senya Polikovsky, Daniel Scharstein, and Michael J Black. Capturing and inferring dense full-body human-scene contact. In *Proceedings of*

- the IEEE/CVF Conference on Computer Vision and Pattern Recognition*, pages 13274–13285, 2022. 1
- [22] Zeng Huang, Yuanlu Xu, Christoph Lassner, Hao Li, and Tony Tung. Arch: Animatable reconstruction of clothed humans. In *Proceedings of the IEEE/CVF Conference on Computer Vision and Pattern Recognition*, pages 3093–3102, 2020. 4
- [23] Sumit Jain and C Karen Liu. Interactive synthesis of human-object interaction. In *Proceedings of the 2009 ACM SIGGRAPH/Eurographics Symposium on Computer Animation*, pages 47–53, 2009. 3
- [24] Vinoj Jayasundara, Amit Agrawal, Nicolas Heron, Abhinav Shrivastava, and Larry S Davis. Flexnerf: Photorealistic free-viewpoint rendering of moving humans from sparse views. In *Proceedings of the IEEE/CVF Conference on Computer Vision and Pattern Recognition*, pages 21118–21127, 2023. 2
- [25] Yuheng Jiang, Suyi Jiang, Guoxing Sun, Zhuo Su, Kaiwen Guo, Minye Wu, Jingyi Yu, and Lan Xu. Neuralhofusion: Neural volumetric rendering under human-object interactions. In *Proceedings of the IEEE/CVF Conference on Computer Vision and Pattern Recognition*, pages 6155–6165, 2022. 2
- [26] Yuheng Jiang, Kaixin Yao, Zhuo Su, Zhehao Shen, Haimin Luo, and Lan Xu. Instant-nvr: Instant neural volumetric rendering for human-object interactions from monocular rgbd stream. In *Proceedings of the IEEE/CVF Conference on Computer Vision and Pattern Recognition*, pages 595–605, 2023. 2
- [27] Angjoo Kanazawa, Michael J Black, David W Jacobs, and Jitendra Malik. End-to-end recovery of human shape and pose. In *Proceedings of the IEEE conference on computer vision and pattern recognition*, pages 7122–7131, 2018. 4, 14
- [28] Bernhard Kerbl, Georgios Kopanas, Thomas Leimkühler, and George Drettakis. 3d gaussian splatting for real-time radiance field rendering. *ACM Trans. Graph.*, 42(4):139–1, 2023. 2, 3, 13, 14
- [29] Muhammed Kocabas, Jen-Hao Rick Chang, James Gabriel, Oncel Tuzel, and Anurag Ranjan. Hugs: Human gaussian splats. In *Proceedings of the IEEE/CVF conference on computer vision and pattern recognition*, pages 505–515, 2024. 2, 3, 4
- [30] Yu Kong and Yun Fu. Human action recognition and prediction: A survey. *International Journal of Computer Vision*, 130(5):1366–1401, 2022. 1
- [31] Youngjoong Kwon, Baole Fang, Yixing Lu, Haoye Dong, Cheng Zhang, Francisco Vicente Carrasco, Albert Mosella-Montoro, Jianjin Xu, Shingo Takagi, Daeil Kim, et al. Generalizable human gaussians for sparse view synthesis. In *European Conference on Computer Vision*, pages 451–468. Springer, 2025. 3
- [32] Hao Li, Dingwen Zhang, Yalun Dai, Nian Liu, Lechao Cheng, Jingfeng Li, Jingdong Wang, and Junwei Han. Gp-nerf: Generalized perception nerf for context-aware 3d scene understanding. In *Proceedings of the IEEE/CVF Conference on Computer Vision and Pattern Recognition*, pages 21708–21718, 2024. 3
- [33] Quanzhou Li, Jingbo Wang, Chen Change Loy, and Bo Dai. Task-oriented human-object interactions generation with implicit neural representations. In *Proceedings of the IEEE/CVF Winter Conference on Applications of Computer Vision*, pages 3035–3044, 2024. 1
- [34] Zhongguo Li, Anders Heyden, and Magnus Oskarsson. Parametric model-based 3d human shape and pose estimation from multiple views. In *Image Analysis: 21st Scandinavian Conference, SCIA 2019, Norrköping, Sweden, June 11–13, 2019, Proceedings 21*, pages 336–347. Springer, 2019. 4
- [35] Siyou Lin, Hongwen Zhang, Zerong Zheng, Ruizhi Shao, and Yebin Liu. Learning implicit templates for point-based clothed human modeling. In *European Conference on Computer Vision*, pages 210–228. Springer, 2022. 4
- [36] Jia-Wei Liu, Yan-Pei Cao, Tianyuan Yang, Zhongcong Xu, Jussi Keppo, Ying Shan, Xiaohu Qie, and Mike Zheng Shou. Hosnerf: Dynamic human-object-scene neural radiance fields from a single video. In *Proceedings of the IEEE/CVF International Conference on Computer Vision*, pages 18483–18494, 2023. 2, 4
- [37] Xian Liu, Xiaohang Zhan, Jiayang Tang, Ying Shan, Gang Zeng, Dahua Lin, Xihui Liu, and Ziwei Liu. Humangaussian: Text-driven 3d human generation with gaussian splatting. In *Proceedings of the IEEE/CVF Conference on Computer Vision and Pattern Recognition*, pages 6646–6657, 2024. 2, 4
- [38] Xinpeng Liu, Haowen Hou, Yanchao Yang, Yong-Lu Li, and Cewu Lu. Revisit human-scene interaction via space occupancy. In *European Conference on Computer Vision*, pages 1–19. Springer, 2025. 1
- [39] Yuan Liu, Sida Peng, Lingjie Liu, Qianqian Wang, Peng Wang, Christian Theobalt, Xiaowei Zhou, and Wenping Wang. Neural rays for occlusion-aware image-based rendering. In *Proceedings of the IEEE/CVF Conference on Computer Vision and Pattern Recognition*, pages 7824–7833, 2022. 7, 14
- [40] Yang Liu, Chuanchen Luo, Lue Fan, Naiyan Wang, Junran Peng, and Zhaoxiang Zhang. Citygaussian: Real-time high-quality large-scale scene rendering with gaussians. In *European Conference on Computer Vision*, pages 265–282. Springer, 2025. 3
- [41] Matthew Loper, Naureen Mahmood, Javier Romero, Gerard Pons-Moll, and Michael J Black. Smpl: a skinned multi-person linear model. *ACM Transactions on Graphics (TOG)*, 34(6):1–16, 2015. 13
- [42] Marko Mihajlovic, Sergey Prokudin, Siyu Tang, Robert Maier, Federica Bogo, Tony Tung, and Edmond Boyer. Splatfields: Neural gaussian splats for sparse 3d and 4d reconstruction. In *European Conference on Computer Vision*, pages 313–332. Springer, 2025. 2
- [43] Ben Mildenhall, Pratul P Srinivasan, Matthew Tancik, Jonathan T Barron, Ravi Ramamoorthi, and Ren Ng. Nerf: Representing scenes as neural radiance fields for view synthesis. *Communications of the ACM*, 65(1):99–106, 2021. 3
- [44] Arthur Moreau, Jifei Song, Helisa Dharmo, Richard Shaw, Yiren Zhou, and Eduardo Pérez-Pellitero. Human gaussian

- splatting: Real-time rendering of animatable avatars. In *Proceedings of the IEEE/CVF Conference on Computer Vision and Pattern Recognition*, pages 788–798, 2024. 3, 4
- [45] Thomas Müller, Alex Evans, Christoph Schied, and Alexander Keller. Instant neural graphics primitives with a multi-resolution hash encoding. *ACM transactions on graphics (TOG)*, 41(4):1–15, 2022. 3
- [46] Avinash Paliwal, Wei Ye, Jinhui Xiong, Dmytro Kotovenko, Rakesh Ranjan, Vikas Chandra, and Nima Khademi Kalantari. Coherentgs: Sparse novel view synthesis with coherent 3d gaussians. In *European Conference on Computer Vision*, pages 19–37. Springer, 2025. 2
- [47] Yik Lung Pang, Changjae Oh, and Andrea Cavallaro. Sparse multi-view hand-object reconstruction for unseen environments. In *Proceedings of the IEEE/CVF Conference on Computer Vision and Pattern Recognition*, pages 803–810, 2024. 1
- [48] Sida Peng, Junting Dong, Qianqian Wang, Shangzhan Zhang, Qing Shuai, Xiaowei Zhou, and Hujun Bao. Animatable neural radiance fields for modeling dynamic human bodies. In *Proceedings of the IEEE/CVF International Conference on Computer Vision*, pages 14314–14323, 2021. 4, 14
- [49] Felix Petersen, Bastian Goldluecke, Christian Borgelt, and Oliver Deussen. Gendr: A generalized differentiable renderer. In *Proceedings of the IEEE/CVF Conference on Computer Vision and Pattern Recognition*, pages 4002–4011, 2022. 3
- [50] Chandradeep Pokhariya, Ishaan Nikhil Shah, Angela Xing, Zekun Li, Kefan Chen, Avinash Sharma, and Srinath Sridhar. Manus: Markerless grasp capture using articulated 3d gaussians. In *Proceedings of the IEEE/CVF Conference on Computer Vision and Pattern Recognition*, pages 2197–2208, 2024. 2, 6, 7, 14
- [51] Zhiyin Qian, Shaofei Wang, Marko Mihajlovic, Andreas Geiger, and Siyu Tang. 3dgs-avatar: Animatable avatars via deformable 3d gaussian splatting. In *Proceedings of the IEEE/CVF Conference on Computer Vision and Pattern Recognition*, pages 5020–5030, 2024. 3
- [52] Xiuquan Qiao, Pei Ren, Schahram Dustdar, Ling Liu, Huadong Ma, and Junliang Chen. Web ar: A promising future for mobile augmented reality—state of the art, challenges, and insights. *Proceedings of the IEEE*, 107(4):651–666, 2019. 2
- [53] Javier Romero, Dimitrios Tzionas, and Michael J Black. Embodied hands: modeling and capturing hands and bodies together. *ACM Transactions on Graphics (TOG)*, 36(6):1–17, 2017. 15
- [54] Javier Romero, Dimitrios Tzionas, and Michael J Black. Embodied hands: Modeling and capturing hands and bodies together. *arXiv preprint arXiv:2201.02610*, 2022. 4
- [55] Umme Sara, Morium Akter, and Mohammad Shorif Uddin. Image quality assessment through fsim, ssim, mse and psnr—a comparative study. *Journal of Computer and Communications*, 7(3):8–18, 2019. 14
- [56] Johannes L Schonberger and Jan-Michael Frahm. Structure-from-motion revisited. In *Proceedings of the IEEE conference on computer vision and pattern recognition*, pages 4104–4113, 2016. 2
- [57] Richard Shaw, Michal Nazarczuk, Jifei Song, Arthur Moreau, Sibi Catley-Chandar, Helisa Dharmo, and Eduardo Pérez-Pellitero. Swings: sliding windows for dynamic 3d gaussian splatting. In *European Conference on Computer Vision*, pages 37–54. Springer, 2025. 2
- [58] Ashwath Shetty, Marc Habermann, Guoxing Sun, Diogo Luvizon, Vladislav Golyanik, and Christian Theobalt. Holoported characters: Real-time free-viewpoint rendering of humans from sparse rgb cameras. In *Proceedings of the IEEE/CVF Conference on Computer Vision and Pattern Recognition*, pages 1206–1215, 2024. 2
- [59] Harry Shum and Sing Bing Kang. Review of image-based rendering techniques. *Visual Communications and Image Processing 2000*, 4067:2–13, 2000. 2
- [60] Aljoscha Smolic, Karsten Mueller, Philipp Merkle, Tobias Rein, Matthias Kautzner, Peter Eisert, and Thomas Wiegand. Free viewpoint video extraction, representation, coding, and rendering. In *2004 International Conference on Image Processing, 2004. ICIP'04.*, pages 3287–3290. IEEE, 2004. 2
- [61] Shih-Yang Su, Timur Bagautdinov, and Helge Rhodin. Npc: Neural point characters from video. In *Proceedings of the IEEE/CVF International Conference on Computer Vision*, pages 14795–14805, 2023. 2
- [62] Guoxing Sun, Xin Chen, Yizhang Chen, Anqi Pang, Pei Lin, Yuheng Jiang, Lan Xu, Jingyi Yu, and Jingya Wang. Neural free-viewpoint performance rendering under complex human-object interactions. In *Proceedings of the 29th ACM International Conference on Multimedia*, pages 4651–4660, 2021. 2
- [63] Xin Suo, Yuheng Jiang, Pei Lin, Yingliang Zhang, Minye Wu, Kaiwen Guo, and Lan Xu. Neuralhumanfvv: Real-time neural volumetric human performance rendering using rgb cameras. In *Proceedings of the IEEE/CVF conference on computer vision and pattern recognition*, pages 6226–6237, 2021. 2, 7, 14
- [64] Omid Taheri, Nima Ghorbani, Michael J Black, and Dimitrios Tzionas. Grab: A dataset of whole-body human grasping of objects. In *Computer Vision—ECCV 2020: 16th European Conference, Glasgow, UK, August 23–28, 2020, Proceedings, Part IV 16*, pages 581–600. Springer, 2020. 5
- [65] Adam Tonderski, Carl Lindström, Georg Hess, William Ljungbergh, Lennart Svensson, and Christoffer Petersson. Neurad: Neural rendering for autonomous driving. In *Proceedings of the IEEE/CVF Conference on Computer Vision and Pattern Recognition*, pages 14895–14904, 2024. 1
- [66] Shashank Tripathi, Agniv Chatterjee, Jean-Claude Passy, Hongwei Yi, Dimitrios Tzionas, and Michael J Black. Deco: Dense estimation of 3d human-scene contact in the wild. In *Proceedings of the IEEE/CVF International Conference on Computer Vision*, pages 8001–8013, 2023. 5
- [67] Qianqian Wang, Zhicheng Wang, Kyle Genova, Pratul P Srinivasan, Howard Zhou, Jonathan T Barron, Ricardo Martin-Brualla, Noah Snavely, and Thomas Funkhouser. Ibrnet: Learning multi-view image-based rendering. In *Proceedings of the IEEE/CVF conference on computer vision and pattern recognition*, pages 4690–4699, 2021. 7, 14

- [68] Zhou Wang, Alan C Bovik, Hamid R Sheikh, and Eero P Simoncelli. Image quality assessment: from error visibility to structural similarity. *IEEE transactions on image processing*, 13(4):600–612, 2004. 6, 14
- [69] Chung-Yi Weng, Brian Curless, Pratul P Srinivasan, Jonathan T Barron, and Ira Kemelmacher-Shlizerman. Humanerf: Free-viewpoint rendering of moving people from monocular video. In *Proceedings of the IEEE/CVF conference on computer vision and pattern Recognition*, pages 16210–16220, 2022. 2
- [70] Markus Worchel and Marc Alexa. Differentiable rendering of parametric geometry. *ACM Transactions on Graphics (TOG)*, 42(6):1–18, 2023. 3
- [71] Qianyi Wu, Xian Liu, Yuedong Chen, Kejie Li, Chuanxia Zheng, Jianfei Cai, and Jianmin Zheng. Object-compositional neural implicit surfaces. In *European Conference on Computer Vision*, pages 197–213. Springer, 2022. 3
- [72] Wenqi Xian, Jia-Bin Huang, Johannes Kopf, and Changil Kim. Space-time neural irradiance fields for free-viewpoint video. In *Proceedings of the IEEE/CVF conference on computer vision and pattern recognition*, pages 9421–9431, 2021. 2
- [73] Zhen Xu, Sida Peng, Chen Geng, Linzhan Mou, Zihan Yan, Jiaming Sun, Hujun Bao, and Xiaowei Zhou. Relightable and animatable neural avatar from sparse-view video. In *Proceedings of the IEEE/CVF Conference on Computer Vision and Pattern Recognition*, pages 990–1000, 2024. 3
- [74] Bangbang Yang, Yinda Zhang, Yijin Li, Zhaopeng Cui, Sean Fanello, Hujun Bao, and Guofeng Zhang. Neural rendering in a room: amodal 3d understanding and free-viewpoint rendering for the closed scene composed of pre-captured objects. *ACM Transactions on Graphics (TOG)*, 41(4):1–10, 2022. 2
- [75] Juze Zhang, Haimin Luo, Hongdi Yang, Xinru Xu, Qianyang Wu, Ye Shi, Jingyi Yu, Lan Xu, and Jingya Wang. Neural-dome: A neural modeling pipeline on multi-view human-object interactions. In *Proceedings of the IEEE/CVF Conference on Computer Vision and Pattern Recognition*, pages 8834–8845, 2023. 2, 5, 6, 7, 14
- [76] Juze Zhang, Jingyan Zhang, Zining Song, Zhanhe Shi, Chengfeng Zhao, Ye Shi, Jingyi Yu, Lan Xu, and Jingya Wang. Hoi-m³: Capture multiple humans and objects interaction within contextual environment. In *Proceedings of the IEEE/CVF Conference on Computer Vision and Pattern Recognition*, pages 516–526, 2024. 3
- [77] Jiawei Zhang, Jiahe Li, Xiaohan Yu, Lei Huang, Lin Gu, Jin Zheng, and Xiao Bai. Cor-gs: sparse-view 3d gaussian splatting via co-regularization. In *European Conference on Computer Vision*, pages 335–352. Springer, 2025. 2, 3
- [78] Richard Zhang, Phillip Isola, Alexei A Efros, Eli Shechtman, and Oliver Wang. The unreasonable effectiveness of deep features as a perceptual metric. In *Proceedings of the IEEE conference on computer vision and pattern recognition*, pages 586–595, 2018. 6, 14
- [79] Chengfeng Zhao, Juze Zhang, Jiashen Du, Ziwei Shan, Junye Wang, Jingyi Yu, Jingya Wang, and Lan Xu. I’m hoi: Inertia-aware monocular capture of 3d human-object interactions. In *Proceedings of the IEEE/CVF Conference on Computer Vision and Pattern Recognition*, pages 729–741, 2024. 1
- [80] Shuaifeng Zhi, Tristan Laidlow, Stefan Leutenegger, and Andrew J Davison. In-place scene labelling and understanding with implicit scene representation. In *Proceedings of the IEEE/CVF International Conference on Computer Vision*, pages 15838–15847, 2021. 3
- [81] Qunjie Zhou, Maxim Maximov, Or Litany, and Laura Leal-Taixé. The perfect match: Exploring nerf features for visual localization. In *European Conference on Computer Vision*, pages 108–127. Springer, 2025. 3
- [82] Zehao Zhu, Zhiwen Fan, Yifan Jiang, and Zhangyang Wang. Fsgs: Real-time few-shot view synthesis using gaussian splatting. In *European conference on computer vision*, pages 145–163. Springer, 2025. 3
- [83] Matthias Zwicker, Hanspeter Pfister, Jeroen Van Baar, and Markus Gross. Ewa volume splatting. In *Proceedings Visualization, 2001. VIS’01.*, pages 29–538. IEEE, 2001. 13

A. Preliminary Knowledge

A.1. SMPL

The SMPL model is architecturally distinguished by its parametric framework for representing the human body [41]. At its core, SMPL utilizes a triangulated mesh composed of 6890 vertices and 13776 triangles, which collectively define the 3D surface geometry of the human form. Underlying this mesh is a skeletal system of 24 joints, hierarchically organized to mimic human articulation. In terms of parameterization, the shape of SMPL is governed by a set of 10 shape parameters ($\beta \in \mathbb{R}^{10}$). These parameters are coefficients derived from Principal Component Analysis (PCA) on a large dataset of 3D human body scans, effectively capturing the primary modes of variation in human physique. Pose articulation is controlled by 72 pose parameters ($\theta \in \mathbb{R}^{72}$). These parameters encode the 3D rotations, using axis-angle representations, of 23 joints relative to their respective parent joints in the kinematic hierarchy. The root joint (pelvis) orientation is implicitly defined by the global coordinate system or managed externally, thus leaving 23 relative joint rotations to be parameterized.

A.2. SMPL-H

The SMPL-H model represents a structural extension of the foundational SMPL framework, particularly in its refined modeling of hand detail. SMPL-H inherits the core body structure from SMPL, retaining the same 6890 vertices for the body mesh and the identical 24 joints for the body skeleton up to the wrists. The key structural enhancement in SMPL-H is the addition of detailed hand models beyond the wrists. Specifically, approximately 3000 vertices are added per hand (roughly 6000 additional vertices for both hands), meticulously representing the geometric intricacies of the hands. Concurrently, the skeletal system is expanded, incorporating 21 additional joints per hand, totaling 42 new hand joints. These augmented joints account for the articulations within each finger (thumb, index, middle, ring, pinky) and within finger segments (typically 3 joints per finger, though the thumb may have 2 or 3, depending on model fidelity), as well as wrist joints, enabling a finer degree of control over hand pose. To animate these hand joints, SMPL-H introduces a dedicated set of hand pose parameters ($\theta_H \in \mathbb{R}^{90}$), with roughly 45 parameters per hand, totaling 90 parameters for both hands. These parameters govern the rotations of the 42 hand joints.

A.3. 3D Gaussian Splatting

In contrast to Neural Radiance Fields (NeRFs), which employ continuous volumetric representations to model entire 3D scenes, 3D Gaussian Splatting (3DGS) leverages a fundamentally different approach. It represents a scene as a collection of discrete, unstructured 3D Gaussians [28]. This

discrete representation offers an alternative to the continuous field learned by NeRFs.

Each 3D Gaussian in this representation is mathematically defined by two key components: a center point \mathbf{p} , denoting its spatial location in world coordinates, and a 3D covariance matrix Σ , which dictates its shape and orientation. The spatial distribution of each Gaussian $G(\mathbf{x})$ is then given by the formula:

$$G(\mathbf{x}) = \frac{1}{(2\pi)^{\frac{3}{2}} |\Sigma|^{\frac{1}{2}}} e^{-\frac{1}{2}(\mathbf{x}-\mathbf{p})^T \Sigma^{-1}(\mathbf{x}-\mathbf{p})} \quad (12)$$

To ensure that the covariance matrix Σ remains positive semi-definite—a crucial condition for it to represent a valid covariance—it is parameterized using a decomposition into learnable components. Specifically, Σ is constructed from a quaternion $\mathbf{r} \in \mathcal{R}^4$, representing rotation, and a scaling vector $\mathbf{s} \in \mathcal{R}^3$. The quaternion \mathbf{r} is converted into a rotation matrix \mathbf{R} , and the scaling vector \mathbf{s} into a diagonal scaling matrix \mathbf{S} . The covariance matrix is then computed as $\Sigma = \mathbf{R}\mathbf{S}\mathbf{S}^T\mathbf{R}^T$, guaranteeing its positive semi-definiteness.

The rendering process in 3DGS involves "splatting" these 3D Gaussians onto the 2D image plane. This process begins by transforming each 3D Gaussian from world coordinates to ray coordinates. Following the methodology outlined in prior work [83], this transformation utilizes a world-to-camera transformation matrix \mathbf{W} , a translation vector \mathbf{d} , and a Jacobian matrix \mathbf{J} . The Jacobian approximates the projective transformation from camera to ray coordinates. In the ray coordinate system, each 3D Gaussian maintains its Gaussian form, but its parameters are transformed. The mean vector \mathbf{p}' and covariance matrix Σ' in ray coordinates are derived from the original world-space parameters \mathbf{p} and Σ as: $\mathbf{p}' = \mathbf{m}(\mathbf{W}\mathbf{p} + \mathbf{d})$ and $\Sigma' = \mathbf{J}\mathbf{W}\Sigma\mathbf{W}^T\mathbf{J}^T$, where $\mathbf{m}(\cdot)$ denotes the mapping from camera to ray coordinates. Subsequently, these transformed 3D Gaussians are projected onto the 2D screen plane. The 2D projection can be efficiently computed by integrating the 3D Gaussian along the projection direction or by leveraging properties detailed in [83].

For image synthesis, the 2D projections of all Gaussians are considered. For each pixel, contributions from all overlapping 2D Gaussians are aggregated. Each Gaussian i contributes a color c_i and an opacity α_i . To composite these contributions and determine the final pixel color \hat{C} , an alpha-blending technique is employed, ordered from front-to-back:

$$\hat{C} = \sum_{i \in N} c_i \alpha_i \prod_{j=1}^{i-1} (1 - \alpha_j). \quad (13)$$

where N denotes the set of Gaussians contributing to the pixel.

The 3DGS method incorporates an adaptive refinement strategy during optimization to enhance rendering quality. Initially, 3D Gaussians are positioned in the scene, typically initialized using Structure-from-Motion (SfM) outputs or random sampling. Subsequently, the algorithm adaptively refines the Gaussian representation through operations of splitting, cloning, and pruning. Gaussians exhibiting large positional gradients are targeted for splitting or cloning. Specifically, a Gaussian may be split into smaller Gaussians if its scaling matrix magnitude exceeds a threshold, or cloned if the scaling magnitude is below a threshold. While splitting and cloning increase the number of Gaussians, a pruning operation concurrently removes redundant Gaussians, specifically those with excessively low opacity (α) or excessively large scale, maintaining efficiency and focusing computational resources on relevant scene regions.

B. Additional Implementation Details

Implementation Details. In general, we adopt a two-stage training procedure for HOGS. In the first stage, we train the sparse-view human pose refinement and the sparse-view human-object contact prediction modules separately. For the sparse-view human pose refinement module, we use the Adam optimizer with a learning rate of $3e-5$ and train for 20 epochs. For the sparse-view human-object contact prediction module, we use the Adam optimizer with a learning rate of $1e-5$ and train for 100 epochs. In the second stage, we perform human-object deformation and composed Gaussian splatting, and further optimize the HOI rendering results within the composed Gaussian splatting framework using physics-aware rendering optimization. More details are shown in the appendix.

Training details. All experiments are carried out on an NVIDIA A100 PCIe GPU. Within the human-object deformation, the LBS modulation module is implemented as an MLP with 5 fully connected layers (an input layer, three hidden layers, and an output layer). Each layer is followed by a ReLU activation function. To enhance the representation of the 3D Gaussian positions, we apply positional encoding before feeding them into the MLP. The MLP maps the 63-dimensional encoded Gaussian positions to 52-dimensional joint offsets, corresponding to the number of joints in the SMPL-H model. The module is optimized using the Adam optimizer with a learning rate of $1e-5$. Other training details for 3D Gaussians (e.g., initialization, densification, pruning, optimization schedule) are the same as in [28].

As for the sparse-view human pose refinement module, the structure of pre-trained CNN follows HMR [27]. The parameters λ_θ and λ_β are set to 1 and 0.001, respectively.

In terms of sparse-view human-object contact prediction module, the single-view contact prediction encoder extracts

per-view features of dimension $D_{\text{DECO}} = 2048$. These features are then aggregated by a cross-view attention module. The input to this module is a tensor $F \in \mathbb{R}^{N \times 2048}$, where $N = 6$ represents the number of input views used in our experiments. Within the attention module, Q , K , and V matrices are computed by linearly projecting the input features F using weight matrices $W_Q, W_K, W_V \in \mathbb{R}^{2048 \times 512}$, respectively. The attention mechanism outputs a tensor $F_{\text{att}} \in \mathbb{R}^{N \times 512}$, which is then averaged across the view dimension to produce a fused feature vector $F_{\text{fuse}} \in \mathbb{R}^{512}$.

With respect to the total loss function, we set $\lambda_{\text{mask}} = 0.3$, $\lambda_{\text{ssim}} = 0.5$, $\lambda_{\text{lpiips}} = 0.1$, $\lambda_{\text{attr}} = 0.01$, and $\lambda_{\text{rep}} = 0.01$, respectively.

Evaluation Metrics. To quantitatively evaluate the quality of rendered novel view and novel pose images, we report the peak signal-to-noise ratio (PSNR) [55], the structural similarity index (SSIM) [68], and the Learned Perceptual Image Patch Similarity (LPIPS) [78].

Details of comparable methods. 1) Mesh-based blending: NeuralHumanFVV [63], a representative mesh-based method that blends textured meshes reconstructed from multi-view images using a neural network to learn blending weights, achieving real-time rendering. This method serves as a baseline to evaluate the advantages of our Gaussian-based representation. 2) NeRF-based rendering: IBR-Net [67] synthesizes novel views by interpolating in a continuous 5D space (position and viewing direction), dynamically drawing information from multiple input views via a network with MLPs and a ray transformer, providing a strong baseline for novel view synthesis. Neuray [39] addresses occlusion issues in novel view synthesis by predicting 3D point visibility from input views, enabling radiance field construction to focus on visible image features for improved rendering quality. NeuralDome [75], achieves high-quality free-view rendering of multi-view human-object interactions by employing a layered NeRF representation, which presents a strong baseline for novel view synthesis. 3) 3DGS-based rendering: we compare with a modified version of MANUS [50], a recent 3DGS-based method designed for markerless grasp capture. MANUS uses articulated 3D Gaussians to represent both the hand and the object, rendering them separately and then combining the results. In our comparison, we replace the hand rendering component of MANUS with an SOTA articulated human rendering method [48], while keeping the object rendering and combination pipeline of MANUS unchanged. This comparison allows us to specifically assess the impact of our proposed HOI rendering approach within the 3DGS framework.

Table 3. Quantitative results on the MANUS-Grasps dataset.

We evaluate HOGS on the MANUS-Grasps dataset to demonstrate generalization to articulated hand-object interactions, comparing with the MANUS.

Method	PSNR \uparrow	SSIM \uparrow	LPIPS \downarrow
MANUS	26.328	0.9872	0.0688
HOGS (Ours)	27.425	0.9891	0.0651

C. Additional Experimental Results

To further demonstrate the extensibility of our proposed HOGS method, particularly for articulated object interactions, we conducted quantitative evaluations on the MANUS-Grasps dataset. We adapted HOGS for hand-object scenarios by replacing the human model with a MANO hand model [53] within the human-object deformation process. As shown in Table 3 HOGS outperforms MANUS on the MANUS-Grasps dataset across all metrics (PSNR, SSIM, LPIPS), demonstrating its effectiveness in rendering articulated hand-object interactions and its strong generalization capability.

D. Limitations and Future Work

Currently, HOGS employs a two-stage training process, requiring separate training of the human pose refinement and contact prediction modules before accurate HOI rendering can be achieved. Future work will explore more efficient single-stage training strategies to streamline the process and potentially improve overall performance. Moreover, this work focuses on single human-object interactions; extending HOGS to handle more complex multi-person multi-object scenarios is a natural extension. Finally, while sparse-view input addresses many practical scenarios, handling monocular input remains an important direction for future research, potentially broadening the applicability of our method.